

An Emission-Line Search for Star-Forming Dwarf Galaxies Toward Abell 851

Crystal L. Martin^{1,2,3}, Jennifer Lotz², Henry C. Ferguson

Space Telescope Science Institute, 3700 San Martin Drive, Baltimore, MD 21218

Received _____; accepted _____

¹Hubble Fellow

²Visiting astronomer Kitt Peak National Observatory The National Optical Astronomy Observatories are operated by the Association of Universities for Research in Astronomy, Inc. under cooperative agreement with the National Science Foundation.

³Present Address: Caltech 105-24, Pasadena, CA 91125

ABSTRACT

We present deep images of the redshift $z = 0.41$ galaxy cluster Abell 851 (Cl 0939+4713) including a narrow bandwidth image of the redshifted [OII] $\lambda\lambda 3726, 29$ line emission. The [OII] doublet is the most accessible tracer of star formation out to redshifts near unity, and we use it to identify candidates for star-forming galaxies. The galaxies selected lie within a projected clustercentric distance of 2 Mpc and have line-of-sight velocities with respect to the cluster in the range between $\pm 1460 \text{ km s}^{-1}$. The sample is complete to magnitude $m_{5129}(AB) = 24.0$ for galaxies with emission-line equivalent widths greater than about 11 Å in the observed frame. The sample is contaminated by foreground galaxies with a steep 4000 Å break across the filters and possibly Ly α emitters at $z=3.31$, but such galaxies can be identified using color, brightness, and equivalent-width criteria. Excluding the likely interlopers, the number density of star-forming galaxies near Cl 0939+4713 is still at least three to four times higher than that of a similar column through the field at $z=0.4$. Galaxies in the cluster sample have lower [OII] equivalent widths than similarly selected field galaxies at $z \sim 0.4$ however, and we suggest that while the density of galaxies is higher in the cluster the star-formation activity in individual galaxies is suppressed relative to their counterparts in the field. The relatively small enhancement in the surface density of the [OII]-selected population toward the cluster core leads us to believe the [OII]-selected galaxies reside in the outer regions of the cluster. We identify a population of starburst galaxies among the [OII]-emitters based on their blue g-i color. The majority of the [OII]-selected galaxies appear to be related to the normal spiral galaxy population, but the bursting population is dominated by intrinsically faint galaxies of below average size. We suggest that this population is composed primarily of dwarf galaxies

and discuss their relation to the dwarf galaxies in present day clusters.

1. Introduction

Cosmological models for the hierarchical growth of structure predict an abundance of low mass galaxy halos. The properties of the dwarf galaxies residing in the halos that survive to the present epoch are extremely sensitive to their star formation histories. A better understanding of how the star formation rate (SFR) evolves in dwarf galaxies is needed to understand their role in the assembly of galaxies.

Most of the dwarf galaxies in the local universe, at least in terms of numbers, are gas-poor galaxies with smooth light distributions whose surface brightness declines exponentially with radius (Ferguson & Binggeli 1994). We refer to these galaxies as dwarf elliptical galaxies or dE’s. This broad class includes the dwarf spheroidal galaxies of the Local Group but not M32-like dwarfs which populate a different locus in the surface brightness vs. magnitude plane (Ferguson & Binggeli 1994, Mateo 1999). The nature of the star-forming progenitors of dE’s, which were not necessarily dwarf galaxies, remains highly controversial. Two factors strongly suggest environment has played a significant role in shaping their star formation history. First, the number of dE’s per giant galaxy increases with the richness of the environment (Ferguson & Sandage 1991). Second, the duration of the inferred quiescent period between bursts of star formation in many dwarf spheroidals is of order 1 Gyr (Smecker-Hane et al. 1994; Grebel 1997). Starburst-driven winds and superbubbles lift gas out of the disks of dwarf galaxies on timescales of 10 to 100 Myr (Martin 1998; Mac Low & Ferrara 1999). Much of this gas is predicted to fall back down on the disk over comparable time periods, so a higher burst frequency is expected from self-regulated star formation. The orbital timescales of satellite galaxies and the frequency of tidal interactions between field galaxies offer a more natural match to the measured burst interval (Moore et al. 1996).

It remains unclear when a typical dE galaxy formed the bulk of its stars, but some of

the progenitors must have been forming stars as recently as $z \sim 0.4$. The isochrones fitted to the color – magnitude diagrams of many local group dwarf spheroidal galaxies provide direct evidence for starbursts a few Gyrs ago (Smecker-Hane et al. 1994; Grebel 1997). Although the color - magnitude relation of the dE’s in nearby clusters has typically been interpreted as evidence that the bulk of their stars formed very early, an intermediate age population in these galaxies would be difficult to detect or distinguish (cf. Thuan 1985; Bothun et al. 1986). But do clusters at moderate redshifts even contain star-forming dwarf galaxies? And, if so, is this population very different from the star-forming population in present epoch clusters? Studying the dynamics of such a population could help characterize the gas removal mechanism.

To date, the dwarf galaxy population in moderate redshift clusters has only been detected as a statistical excess of faint galaxies relative to the field (Driver et al. 1994; Wilson et al. 1997; Trentham 1997b; Trentham 1998). Dressler et al. (1999) and Dressler & Gunn (1982) describe extensive spectroscopic surveys of Abell 851 (Cl 0939+4713), but their completeness limits are not yet deep enough to describe the dwarf galaxy population well. Dressler et al. (1999) recovered cluster members in one out of every two spectra to $m \approx 22$, but the efficiency of this direct approach will decline toward fainter flux levels. (The number of background galaxies rises more steeply with magnitude than the number counts of cluster galaxies are likely to increase with magnitude.) Once cluster members have been identified at $V = 22$ to $V = 24$, spectroscopy with 10 m class telescopes can be used to study their properties. For example, Koo et al. (1997) find the emission-line widths of three (possibly four) of the six compact galaxies observed so far in Cl0024+1654 are quite narrow; and Kobulnicky et al. (1999) report measurements of the O/H abundance ratios for two of these galaxies.

Since a large fraction of cluster galaxies at $z \sim 0.4$ have experienced recent star

formation (Butcher & Oemler 1978; Dressler & Gunn 1982), emission-line selection would appear to be an efficient means of identifying the faint cluster members. To find these emission-line galaxies over regions much larger than the cluster core, we have undertaken a deep narrowband imaging survey of moderate-redshift clusters. One filter isolates redshifted [OII] $\lambda\lambda 3726, 3729$ emission line radiation from galaxies near the mean cluster redshift, and the continuum is measured in a second deep image. The main advantage of the [OII] line is that it remains in the optical region out to redshifts of $z \sim 1$. The major limitation of this method is the limited accuracy of [OII] as a tracer of the number of young massive stars. Fortunately, the [OII] flux from nearby galaxies correlates with their $H\alpha$ luminosity, which is a direct measure of the SFR (Gallagher et al. 1989; Kennicutt 1992; Loveday et al. 1999). The scatter in this relation and uncertainty regarding the amount of attenuation from dust in the galaxies limit how accurately we can estimate SFRs for the objects we find, but the method does identify a much larger sample of candidates for follow-up studies than has previously been available.

In this paper, we discuss our selection technique and present results for the cluster Abell 851, also known as Cl 0939+4713. This extraordinarily rich cluster contains 160 members to $R = 22.5$ (Belloni & Roeser 1996), and its X-ray luminosity approaches that of the Coma cluster (Sadat 1998). Dressler et al. (1999) present spectra for 71 cluster members and derive a mean redshift of $z = 0.4060$ and cluster velocity dispersion of $\sigma = 1260 \text{ km s}^{-1}$. The cluster core contains a high fraction of blue galaxies, and many of these have irregular morphologies (Dressler et al. 1994; Smail et al. 1997). Our observations of this cluster and the resulting sensitivity to line emission are described in §2. Sample contamination from other spectral features is discussed in §3 prior to comparing the cluster galaxies to the [OII]-selected population of field galaxies. In §4 we discuss the star formation histories of the [OII] selected galaxies, argue that some of these galaxies are dwarf galaxies in a starburst phase, and speculate about the nature of their remnants. Our conclusions are

summarized in §5.

2. Data

2.1. Observations

Images of Abell 851 were obtained using the T2KB CCD and prime focus camera on the KPNO 4m telescope on the nights of 1998 January 23-26. Filter W022 was chosen as the redshifted [OII] filter based on the redshift and cluster velocity dispersion published by Dressler & Gunn (1992) which are 0.4067 and 860 km s⁻¹, respectively. The revised redshift from Dressler et al. (1999) still places the cluster in the center of this bandpass, but the larger velocity dispersion means our survey is less complete than we originally intended.⁴ Figure 1 shows the effective transmission curve of W022 in the f/3.14 prime focus beam. Using the revised value $\sigma = 1260$ km s⁻¹, the peculiar velocity of a galaxy with respect to the cluster must be between -1.17σ and 1.15σ for the [OII] line to be redshifted into the region of filter W022 where the transmission is greater than 70%. Roughly 75% of the virialized cluster galaxies should be detected by our survey. Note, that this redshift interval samples a much larger proper distance than the angular diameter distance subtended by our field, which is ~ 4 Mpc on a side at $z = 0.4$.⁵ We chose a continuum filter W021 with a central wavelength at $\lambda 5129$ Å, which is 116 Å blueward of the center of the on-band filter.

The individual frames were bias subtracted, corrected for pixel-to-pixel sensitivity variations, and corrected for the large-scale illumination pattern. An iterative cosmic-ray rejection algorithm, CRREJ in IRAF, was then used to combine the photometric frames in

⁴Note that the velocity dispersion listed in Dressler & Gunn (1992), 860 km s⁻¹, should be 1060 km s⁻¹ for the data presented there.

⁵ All calculations in the paper assume $H_0 = 70$ km s⁻¹ Mpc⁻¹; $q_0 = 0.1$.

each filter. The telescope was offset $60''$ between pairs of exposures in a pattern that makes the exposure time constant over most of the $14'3$ field of view. The total exposure time in the photometric on-band and off-band frames was 13,200 s and 10,800 s, respectively. The photometric images were flux calibrated with observations of Kitt Peak spectrophotometric standards (Massey et al. 1988). More images were taken under good, but not photometric, conditions bringing the total exposure time in each band to 18,000 s. The sum of these deeper images is shown in Figure 2. The region shown is the central $1/9$ th of our field, and the remainder of the field can be viewed at <http://astro.caltech.edu/~clm/dwoii.html>. The count rates were a few percent lower than in the photometric images, so we scaled the sensitivity by the mean count ratio of the 1000 brightest objects. The standard deviation of this distribution of flux ratios was added in quadrature to the uncertainty in the original flux calibration, and this value was used as the uncertainty in the flux calibration of the deep images. The root-mean-square (RMS) variations in the sky brightness is $\sigma_{sky} = 2.11 \times 10^{-18}$ ergs s $^{-1}$ cm $^{-2}$ arcsec $^{-2}$ and 4.1×10^{-18} ergs s $^{-1}$ cm $^{-2}$ arcsec $^{-2}$ in the on-band and off-band images, respectively. The seeing, as measured with the IRAF task IMEXAMINE, was $1''.2$ FWHM (full width at half maximum intensity).

Broadband images were also obtained on the night of 1998 January 26 through the standard Sloan g and i filters (Fukugita et al. 1996). The total exposure time in each band was 1 hour. Conditions were partly cloudy and the net image quality was $2''.2$ FWHM in g and $2''.5$ FWHM in i. The reduction of these images was similar to that of the narrowband images. An acceptable g-band calibration, root-mean-square (RMS) scatter of 0.22 mag., was obtained from published Gunn magnitudes (Dressler & Gunn 1992) and the transformations described by Jorgenson (1994) and Fukugita et al. (1996). Our i-band photometry was calibrated using new measurements of calibrated WFPC2 F814W frames that were obtained from the HST archive. We used the typical magnitude differences between these two sets of photometry, an RMS value of 0.17 mag., to estimate

the uncertainty level of the flux calibration.

2.2. Detection and Photometry

The combined W022 and W021 image was convolved with a gaussian of FWHM=4.0 pixels and searched for groups of three or more connected pixels each with signal greater than $1.5\sigma_{sky}$ using SExtractor (Bertin & Arnouts 1996). A total of 5842 objects were detected, and nearly all detections included 5 or more pixels. Only one source was detected on the inverse image using the same parameters, so the false detection rate is believed to be quite low. Sources found within ~ 10 pixels of the edge of the field were omitted from the catalogs reducing the total area surveyed to 181 arcmin². A background map was generated for each frame by fitting a smooth surface to a mesh of the local median sky values. Thirty pixel by 30 pixel cells proved large enough to remove objects and provided sufficient resolution to model residual scattered light.

Apertures were defined at a constant isophotal brightness on the summed narrowband images. After convolving the g and i images to the FWHM image quality of the i image, isophotal magnitudes were tabulated in g and i as well as W021 and W022 using SExtractor. Errors in the mean background are not included in the magnitude error returned by SExtractor, which includes only the pixel-to-pixel variations in the sky level and poisson noise. Comparison of a range of acceptable background maps showed only a few pixels with discrepancies of several counts. The error introduced by the uncertainty in the mean background level is less than 10% of the error from the pixel-to-pixel fluctuations, $\sqrt{A\sigma_{sky}^2}$, in all but a couple of the largest galaxies.

Figure 3 illustrates how stars were distinguished from small galaxies. The distribution of source sizes over the full range of source brightness is clearly bi-modal. We classified 89

objects as stars based on the concentration of their flux and a model fitted to the point-spread-function of the image. They are represented by circles in Figure 3. These objects are unresolved on the ground-based images, and the two that fall on the HST field are clearly stellar. This distinction becomes ambiguous fainter than $F_\lambda = 10^{-17}$ ergs s⁻¹ cm⁻² Å⁻¹, or $m = 21.5$ AB magnitudes, but the stars at those magnitudes are greatly outnumbered by galaxies. The areal density of bright stars is consistent with the measurements of Jones et al. (1991).

2.3. Sensitivity to Emission Lines

We refer to excess on-band flux (relative to the off-band flux) as *line flux* since [OII] emission at the cluster redshift will be redshifted into the W022 filter. We will discuss other spectral features that might produce an on-band excess in the next section. Scaling the flux in the off band to the effective width of the on-band, the transmitted line flux is given by

$$T(\lambda_l)F_l = F_{ON} - F_{OFF} \int^{ON} T(\lambda) d\lambda / \int^{OFF} T(\lambda) d\lambda,$$

where the error on $T(\lambda_l)F_l$ includes the photometric and calibration errors. The true line flux, F_l , depends on the value of the filter transmission, $T(\lambda_l)$, at the wavelength of the redshifted emission from a particular galaxy. The mean filter transmission is 78% over the bandpass with $T_\lambda > 0.70$. The measurement error includes shot noise from the galaxy plus sky, the pixel-to-pixel fluctuations in the background level, and the uncertainty in the flux calibration. For each detected galaxy, Figure 4 shows the significance of the on-band excess, TF_l , with respect to the standard deviation of the measurement error, σ . Most of the 5560 galaxies detected cluster about the line where this signal-to-noise ratio is zero. They show no excess emission in the on-band, and those near the cluster redshift do not have significant [OII] line emission.

Galaxy detection depends on the total line plus continuum flux in the co-added bandpasses, but the certainty with which we can detect an emission line depends on the contrast between the line and the continuum. The observed equivalent width, $EW_o \equiv TF_l/F_\lambda$, describes this contrast. (Recall that the galaxy’s rest frame spectrum, EW_e , is a factor of $1 + z$ higher.) In Figure 4, the solid lines illustrate the signal-to-noise (S/N) expected for galaxies with equivalent widths of 300 Å, 60 Å, and 11 Å. At fixed equivalent width and angular size, the S/N ratio increases as the square root of the continuum flux up to the brightness where the uncertainty in the flux calibration begins to dominate the measurement error. For a bright galaxy, the significance level of an on-band flux excess depends almost entirely on the line equivalent width. For example, Figure 4 shows that a cut at $S/N = 4$ is equivalent to an equivalent width cut at 11 Å. A cut at $S/N = 3$, dotted line, stretches the equivalent width limit to 8 Å. This limiting equivalent width describes our selection function for galaxies brighter than $F_\lambda = 10^{-18}$ ergs s⁻¹ cm⁻² Å⁻¹ which corresponds to $m_{5129}(AB) = 24.0$. Fainter than this completeness limit, the limiting equivalent width is higher. The size of a faint galaxy also influences the significance of a line detection. As illustrated by curve *b* and curve *c* in Figure 4, compact galaxies are detected at slightly higher significance at a given equivalent width and magnitude.

The S/N ratio of the on-band flux excess exceeds three for 371 galaxies, and these objects define our *on-band-selected sample* of emission-line candidates. A more conservative cut, at say $S/N = 4$, would reduce the number of emission-line candidates to 258. The preferred cut depends upon how the sample is to be used, so we provide the entire $S/N \geq 3$ catalog to allow other researchers to choose a selection level appropriate to their goal. Based on the relative distribution of positive and negative detections in Figure 4, we felt the cut at $S/N = 3$ was appropriate for spectroscopic follow-up. The population of 106 objects with a significant, i.e. $S/N \geq 3$, flux excess in the off-band defines our *off-band selected sample* of galaxies.

Table 1 lists 33 on-band-selected galaxies with colors bluer than $g-i = 1.0$. These candidates for [OII]-emission are ordered by the significance of their on-band flux excess, $T_\lambda F_\lambda / \sigma$, from highest to lowest. Similar tables for galaxies with redder colors are available at <http://astro.caltech.edu/~clm/dwoii.html>. The catalog number (col. 1) is related to a galaxy’s position in our field (cols. 2 and 3). The origin is at the southeast corner of our frame. We fitted a coordinate transformation to an image extracted from the Digitized Sky Survey to derive the absolute positions shown in columns 4 and 5. The root mean square deviation of the fit residuals was $0''.2$. The on-band flux excess is given in col. 6, and col. 7 lists the continuum flux. Cols. 8 and 9 give the broad band flux and color. The nature of these objects is discussed in § 3.

2.4. Star Formation Rate Estimates

To gain some insight into the SFR’s of the [OII]-selected galaxies, we must adopt an empirical relation between the measured [OII] and $H\alpha$ fluxes of the galaxies. The $H\alpha$ luminosity of a galaxy provides an excellent measure of the massive SFR because the recombination rate of the interstellar gas directly reflects the ionization rate. Collisions between the same free electrons and singly ionized oxygen atoms produce the excited states that decay via the [OII] $\lambda\lambda 3726, 29$ transitions. It is therefore not surprising that the [OII] and $H\alpha$ fluxes are correlated (e.g. Gallagher et al. 1989; Kennicutt 1992a, Loveday et al. 1999). The empirical relation among the bluest local galaxies shows a scatter of a factor of three about the mean [OII] versus $H\beta$ relation, $F_{[OII]} = 3.2F_{H\beta}$ (Gallagher et al. 1989). In the absence of reddening, the equivalent [OII] – $H\alpha$ relation would be $F_{[OII]} = 1.17F_{H\alpha}$ assuming a nebular temperature of 10^4 K and Case B recombination (Osterbrock 1989). Throughout this paper we adopt $A_B = 1.0$ as a representative extinction correction for dwarf irregular galaxies (e.g. Martin 1997), and the reddened $H\alpha$ flux is predicted to

be $1.17F_{[OII]}$. This approximation will systematically underestimate the SFR's of spiral galaxies because their fitted $F_{[OII]}/F_{H\alpha}$ ratio is slightly lower (Kennicutt 1992a; Loveday et al. 1999).

Our estimate of the $H\alpha$ flux needs to be corrected for dust attenuation before the $H\alpha$ luminosity, $L_{H\alpha}$ is used to estimate the SFR. The variation in the dust attenuation from galaxy to galaxy is probably at least as large as the differences in the intrinsic $[OII]/H\alpha$ ratio. After the extinction correction, $A_B = 1.0$ mag ($A_{H\alpha} = 0.59$ mag), is applied, the extinction-corrected $H\alpha$ fluxes are 2.0 times larger than the measured, reddened $[OII]$ fluxes. Choosing an extinction correction appropriate for dwarf irregular galaxies will systematically underestimate the attenuation (and SFR) in more luminous galaxies. The SFR calibration derived by Kennicutt et al. (1994) assumes stellar masses from 0.1 to $100 M_{\odot}$ populate the K83 IMF (Kennicutt 1983) and evolve along evolutionary tracks from Schaller et al. (1992). Applying their calibration, $R = L_{H\alpha}/1.36 \times 10^{41} \text{ ergs s}^{-1} M_{\odot} \text{ yr}^{-1}$, to the galaxies with blue colors in Table 1, we find that half of these galaxies have star formations rates less than $0.2 M_{\odot} \text{ yr}^{-1}$. The median SFR in the galaxies with intermediate colors is more than twice as large.

2.5. Incompleteness

We ran Monte Carlo simulations in which artificial images were created with a similar number of galaxies and the same noise as the data. We extracted sources from these images with SExtractor using the parameter settings that had been tuned to the real data. Comparisons between the resulting catalogs and input lists revealed which galaxies were missed. By repeatedly adding several thousand galaxies to the images at a time, we measured the detected fraction of galaxies at each point across a grid of line fluxes and continuum fluxes. We used this grid to assign a detection probability, p_{ij} , to each galaxy.

The galaxies that we added to the images were viewed at random inclinations, but all had exponential surface brightness profiles with a scale length of 1 kpc ($0''.2$). The detection probabilities were not sensitive to the scale length adopted.

Contours of 85% and 3% completeness are superposed on the on-band-selected sample in Figure 5. Galaxies with the same equivalent width lie along diagonal lines in this diagram. Bright galaxies, on the right half of the diagram, are shown down to an equivalent width $EW_o \sim 8 \text{ \AA}$. The simulations do a good job of predicting the break in the data near $\log F_\lambda = -18$, i.e. $m_{5129}(AB) = 24.0$, where the equivalent width limit begins to increase as the galaxies become fainter. Galaxies are detected up to 1.25 magnitudes fainter if their line flux is stronger than $EW_o \sim 30 \text{ \AA}$. Some small fraction of the strong lined objects at $m \approx 27$ are detected, but the continuum is poorly defined.

3. Properties of the [OII]-Selected Galaxy Population

Considering the wide range of redshifts probed by an image of this depth and the complexity of galaxy spectra, demonstration of an on-band flux excess is not an immediately compelling argument for [OII] emission. We use the properties of the on-band selected galaxies and some basic information about the field galaxy population to draw some conclusions about the contamination from spectral features other than the [OII] doublet. The population believed to be [OII]-selected is then compared to the field population, and the distribution of star formation rates is discussed.

3.1. The [OII] Line-Emission or Interloper Question

3.1.1. Emission-Line Interlopers

Our on-band filter (W022) will pick up the [OIII] $\lambda\lambda 4959, 5007$ doublet and the $H\beta$ emission lines from galaxies near redshifts of 0.05 and 0.08, respectively. The volume probed for [OIII] and $H\beta$, however, is only 62 Mpc^3 and 68 Mpc^3 , respectively. Emission line surveys at $z \sim 0.1$ find roughly one galaxy per 25 Mpc^{-3} (Salzer 1989), so we expect less than 5 foreground galaxies to be selected. The comoving volume from which redshifted [OII] emission is selected is 10 times larger. Since the comoving density of emission-line galaxies also increases from $z=0.1$ to $z=0.4$, clearly few foreground galaxies will be found.

The redshift interval of our survey does probe a large volume at high-redshift, and the issue becomes whether the galaxies are bright enough to detect in our survey. The luminosity function of the $z \sim 3$ Lyman-break-selected population turns down at apparent magnitudes brighter than $\mathfrak{R} \sim 24.5$ (cf. Fig. 8 Steidel et al. 1999a). These galaxies have $G - \mathfrak{R}$ colors ranging from 0 to 2, so most $\text{Ly}\alpha$ detections will be from objects fainter than the completeness limit of our survey, $G \approx m_{5129}(AB) \approx 24$. Figure 5 shows the lowest equivalent widths detected at $m_{5129} = 26.5$ and $m_{5129} = 29$ were 60 \AA and 400 \AA , respectively. About 20% of the high-redshift galaxy population have rest-frame $\text{Ly}\alpha$ equivalent widths $\geq 20 \text{ \AA}$ —i.e. EW_o exceeding $\sim 80 \text{ \AA}$ (Steidel et al. 1998; Steidel et al. 1999b). Hence some $z \sim 3.31$ galaxies with strong $\text{Ly}\alpha$ emission must be included in our catalog, but weaker lines like CIII] $\lambda 1909$, or MgII $\lambda 2798$ will be much less common.

The deepest $\text{Ly}\alpha$ surveys find about 30 high-redshift galaxies over volumes comparable to that probed by our on-band (Cowie & Hu 1998; Hu, Cowie, & McMahon 1998). The sensitivity of our survey is lower, so we expect a smaller number of high equivalent-width $\text{Ly}\alpha$ emitters in our sample. To a similar equivalent width limit, $EW_o = 100 \text{ \AA}$, our on-band-selected catalog contains only seven objects. These seven objects could all be [OII]-emitting galaxies in the cluster, however. Their rest-frame equivalent widths would

be less than 285 Å. Galaxies have been found with [OII] equivalent widths as high as 264 Å (Sullivan et al. 1999), and widths of 100 Å are fairly common (e.g. Cowie et al. 1996; Hammer et al. 1997; Balogh et al. 1997; Hogg et al. 1998; Tresse et al. 1999; Gronwall 2000). The Ly α candidates can be distinguished from the high-equivalent width [OII] galaxies using the Lyman break (Lotz & Martin 2001), but a deep u-band image has not been obtained for Abell 851. Our incompleteness function lacks the resolution to accurately estimate the Ly α contamination because the surface density of Ly α emitters is rising steeply in the magnitude range where our sensitivity is dropping sharply. We can conclude that the number of high-redshift Ly α interlopers in the on-band-selected sample is small regardless of the identity of the high-equivalent width lines. The influence of Ly α emitters on the inferred [OII] equivalent width distribution is discussed further in § 3.2.3.

3.1.2. *Continuum Interlopers and Broadband Colors*

The slope of a galaxy’s continuum spectrum can produce a false equivalent width because the continuum is measured blueward of the on-band. However, the g and i band fluxes place important constraints on the degree of contamination. To investigate the magnitude of the errors, we redshifted spectra of real galaxies (from our own collection, the spectral atlas of Kennicutt (1992b), and the composite spectra of Coleman, Wu, & Weedman 1980) and “observed” them in our four bands using the SYNPHOT package in IRAF. Figure 6 illustrates the changes in apparent on-band excess as a function of redshift for the Coleman et al. (1980) representations of E/S0, Sbc, and Im galaxy spectra. Weak [OII] lines in the Im and Sbc templates show up at $z=0.407$ as designed, but the 4000 Å break in some foreground galaxies and the Lyman break in high-redshift galaxies also produce a detectable signal. The broadband colors – shown in the top panel of Figure 6 – provide a means of distinguishing interlopers from [OII]-emitters.

For example, early-type galaxies falling within several redshift intervals between $z=0$ and $z=1$ produce an on-band flux excess exceeding $EW_o = 10 \text{ \AA}$ but can be recognized by their red $g-i$ color which exceeds 2.0. Our catalog contains 123 on-band-excess galaxies with $g-i > 2$, so the fraction of these which are actually interlopers does affect the statistics of the [OII]-selected population. The false equivalent width only exceeds $\sim 20 \text{ \AA}$ when the steepest part of the break which is caused by metal lines in cool giants is redshifted across the filter pair. The expected number of early-type galaxies within this redshift slice at $z \sim 0.3$ is of order ~ 12 (Lilly et al. 1995). The number of interlopers with false $ew \sim 10 \text{ \AA}$ is much larger since galaxies from a much larger volume contribute. We find 15 red galaxies with an on-band excess exceeding 30 \AA . The number increases to 48 red galaxies down to an equivalent width limit of 20 \AA and to 116 down to $EW_o = 10 \text{ \AA}$. Either some of the red galaxies actually are cluster galaxies with [OII] emission or the interloper equivalent width distribution is offset by about 10 \AA to higher equivalent width than our simulations predict. Given the wide variety of observed galaxy spectra, either interpretation is plausible. We conclude that some of the red objects in the on-band selected sample must be interlopers but cannot reliably determine the fraction.

The Lyman discontinuity enters the off-band at $z=4.56$ and exits the on-band at $z=4.77$ in Figure 6. The $g-i$ color of this population is quite red like the 4000 \AA break interlopers, but the magnitude of the signal is much larger. The intrinsic break is only about 70 \AA for a pure O-star population but becomes much larger if B stars dominate the continuum (Leitherer et al. 1999). Absorption by intergalactic gas along the sightline steepens the break further and has been included in Figure 6 (Madau 1995). Since we find no high EW red galaxies, the Lyman discontinuity must not produce any interlopers in our sample.

3.1.3. Spectroscopic Test of the [OII]-Selected Sample

The validity of our technique can be checked by direct comparison to the spectra recently published by Dressler et al. (1999). They find 71 cluster members among spectra of 137 objects in their Abell 851 field but detect the [OII] emission line in only 19 of these members. Six of these 19 galaxies have equivalent widths below our sensitivity limit, and the redshifts of four galaxies are outside the limits of our filter bandpass (see § 2.1). Hence our sample should have nine galaxies in common with the D99 sample. We identified eight of these galaxies as [OII] emitters. The spectrum of the galaxy, D99-#52, that we missed is unusual in that it shows a strong emission line shortward of [OII], and this line happened to fall in our continuum band!⁶ Figure 7 compares our measurements of the [OII] equivalent width to those of D99. The agreement is excellent except for one object, D99-#48, for which we detected only 25% of the line flux. Examination of this spectrum shows the [OII] line fell on the edge of the filter bandpass where the transmission had dropped to $\sim 55\%$. The root mean square deviation for the other 7 points is 6 Å.

The false detection rate was examined for the 52 cluster galaxies with no [OII] emission and the 66 field galaxies. We measured an on-band excess for 8 of these but flagged 6 of them as steep spectral breaks rather than [OII] emission due to their red color (see § 3.1.2). The other two had colors nearly as red as the limit we used to make this distinction. The detection algorithm missed 3 galaxies that were located very close to bright foreground stars. We measured no on-band excess for the other 104 objects. This comparison, summarized in Table 2, demonstrates that the selection function of our survey is well understood to $m_R(AB) \sim 22$. Since the nature of systemic errors from interlopers changes

⁶ This line is near the wavelength of HeI 3554 from the galaxy, but it is much stronger than expected for HII galaxies. The presence of this line in our continuum band explains why we measured a weak off-band excess for this [OII] emitting galaxy.

with magnitude, the method should be tested spectroscopically $m(AB) \sim 25$.

3.2. Comparison to the [OII]-Selected Field Population

Encouraged by the agreement with the published spectra, we consider the galaxies selected in the on-band with $S/N \geq 3$ good candidates for [OII] emission if their g-i color does not exceed 2.0. This color cut excludes 123 galaxies leaving 248 galaxies in the [OII]-selected sample. Direct comparisons to the [OII]-selected population of field galaxies near $z \sim 0.4$ (Hogg et al. 1998 and Cowie et al. 1997) are complicated by differences in selection criteria. However, internal comparisons to the off-band selected emission line galaxies can be used as a cross-check on the comparison to the field population of [OII]-emitting galaxies.

3.2.1. The [OII] Luminosity Function

In Table 3 the galaxies from the [OII]-selected sample have been divided into four line flux intervals. This method of counting adds faint galaxies with strong line emission to the same bins as bright galaxies with weak line emission, so the affect of the survey selection function on the counts is not immediately apparent. We used the simulations described in § 2.5 to measure the probability, p_{ij} , of detecting a galaxy with magnitude i and line flux j . The number counts are then corrected by the number of missed galaxies per detected galaxy, where this factor is defined by the sum, $1/N \sum 1/p_{ij}$, over all the galaxies in a bin containing N galaxies. The correction factor for each flux bin is listed in column 5. The error estimate reflects the dispersion among several sets of simulations. We find that these observations provide a robust measurement of the number of [OII]-emitting galaxies down to star-formation rates $\sim 0.3 \text{ M}_{\odot} \text{ yr}^{-1}$ and rest frame equivalent widths exceeding 8 Å. The

counts are determined at the factor of two level down to approximately $0.09 \text{ M}_{\odot} \text{ yr}^{-1}$, but corrections for galaxies fainter than the completeness limit of our survey strongly influence the number density in the lowest SFR bin.

The resulting distribution of star formation rates is shown in Figure 8. The SFR scale includes a mean correction for the filter transmission at the wavelength of the detected line – i.e. the measured $T_{\lambda}F_{[\text{OII}]}$ was divided by the average filter transmission $\bar{T}_{\lambda} = 0.78$ over the bandpass. The exact redshift of a particular galaxy within this interval $z = 0.407 \pm 0.0069$ has only a small effect on the its inferred luminosity. While the narrow-band filter measurements appear to provide a robust measurement of the reddened [OII] luminosities, differences in the excitation among spiral and irregular galaxies create uncertainties in the conversion to SFRs at the level of a factor of 2 to 3. Some galaxies will certainly be much more heavily obscured by dust than the mean irregular galaxy, and their star formation rates would be severely underestimated in the present analysis. Until more robust measures of total SFR can be obtained for these galaxies, we can only assume that the adjustments will shift the overall scale of the SFRs and not their relative distribution.

To normalize the distribution in Figure 8 we integrated the volume subtended by our field over the redshift interval where the on-band filter transmits [OII] emission. Dividing the corrected number counts by this comoving survey volume, 1305 Mpc^3 , provides an estimate of the comoving density of galaxies at each SFR as illustrated by the solid circles in Figure 8. For comparison, the Hogg et al. (1998) [OII] luminosity function is shown to illustrate the density of field galaxies at $z \sim 0.4$. It agrees quite well with the number density of [OII]-emitting galaxies found by our off-band selected sample of emission-line galaxies (open circles). The comoving density of [OII]-selected galaxies is clearly a factor of three to four higher near Abell 851 than it is in the field at similar redshift. This contrast is larger than the increase seen in the field from $z \sim 0$ to $z \sim 0.4$ where the former is

illustrated by the $H\alpha$ derived SFR distribution of Tresse et al. (1998) and Gallego et al. (1995) in Figure 8. Aside from normalization differences, the shape of the SFR distribution in the Abell 851 sample is very similar to that measured for the field galaxies. Inspection of columns 3 and 4 in Table 3 reveals that had we included the red galaxies with an on-band excess the shape of the luminosity distribution would not be significantly affected although the overall normalization would be up by about 50%. The overdensity is 70% as large when only the objects detected at $S/N \geq 4$ are included in the analysis, and this difference provides at least some indication of how much the magnitude of the overdensity might change when our spectroscopic follow-up is completed.

The peculiar motions of cluster galaxies clearly limit the accuracy with which the volume density of star-forming galaxies can be estimated. If the velocity distribution of the cluster galaxies is described by a gaussian distribution, then the random motions of 25% of the cluster galaxies will effectively remove them from our sample raising the true density contrast with the field to a factor of five. The chosen width of the on-band filter still represents a much longer distance along the sightline than the transverse size of our field, so our redshift slice may overestimate the volume in which the cluster galaxies reside. The field subtended at the cluster redshift is 4.10 Mpc by 3.98 Mpc which is about 2 Abell radii across ($R_A = 1.5h^{-1}$ Mpc ≈ 2.1 Mpc = 7'.1). Suppose, for purposes of illustration, that all the [OII]-selected galaxies lie within a volume whose depth along the sightline is also $2R_A$. Then the comoving overdensity of star-forming galaxies increases to a factor of ~ 42 . The projected density of [OII]-selected galaxies at the outer edge of our field can be used to determine whether the overdensity of [OII]-selected galaxies is likely to be confined to a region with dimensions of only ~ 4 Mpc however.

3.2.2. Spatial Distribution

The top and bottom rows of Figure 9 show the spatial distribution of the on-band and off-band selected galaxies respectively. The comoving volume probed by the off-band is 1.89 times larger than the on-band survey volume, so the density contrast between the top and bottom panels is nearly twice as large as the contrast in galaxy counts. At clustercentric radii of ~ 2 Mpc the cluster counts remain higher than the field counts, so the scale of enhanced counts of [OII]-selected galaxies must be larger than 4 Mpc. We estimate that the virial radius of Abell 851 is ~ 4.6 Mpc,⁷ so it seems reasonable that the field counts might not be recovered within our field.

The radial gradient in the surface density of [OII]-selected galaxies is not very steep, so the star-forming galaxies are not strongly clustered. The projected density of star-forming galaxies in the inner half of our field is only 1.45 ± 0.15 times higher than in the outer half. The clustering properties do not change significantly when only the sources detected at $S/N \geq 4$ are included. The radial surface density profile for a virialized population of galaxies would fall much more steeply with radius. The lack of a strong central concentration does not, however, demonstrate that this population is not virialized. Star formation is believed to be strongly suppressed in the galaxies that pass through the core of the cluster, so galaxies would likely become unrecognizable as members of this population

⁷ Estimates of the virial radius for Abell 851 are uncertain due to the substructure in the X-ray emission (Schindler & Wambssann 1996). We modeled the halo as a singular isothermal sphere truncated at the virial radius. Taking an isotropic velocity dispersion (1260 km s^{-1}), we find a cluster virial mass $M_V = 1.0 \times 10^{15} M_\odot (R_V/R_A \sigma_{1000}^2)$. Following the collapse of a spherical perturbation, White et al. (1993) find an overdensity of $(\rho - \rho_0)/\rho = 178 \Omega_0^{-0.6}$ at virialization which corresponds to a cluster mass $M_V = 6.9 \times 10^{14} h^{-1} M_\odot (R_V/R_A)^3 \Omega^{0.4}$. The only virial radius consistent with both these mass estimates is $R_V \approx 2.1 R_A \approx 4.6$ Mpc.

in the cluster core. A measurement of the redshift distribution of the [OII]-selected galaxies will better determine the dynamics of this population.

The spatial distribution of on-band selected galaxies does show more structure than the off-band selected sample in Figure 9. The galaxies with intermediate colors, shown in the middle panel, have concentrations near positions (1000,1000), (850,1300) and (900,250) which form a filament running roughly north – south across the field. The number of galaxies with blue colors is too low to determine if they are as clustered, but several are located near the clumps at (1000,1000) and (900,250). The apparent concentration of red galaxies along the vertical filament in Figure 9 disappears when selection is made at $S/N \geq 4$ instead of $S/N \geq 3$, so we find no significant structure in the distribution of galaxies with red g-i color.

3.2.3. *Equivalent-Width Distribution*

Abell 851 is an extraordinarily rich cluster, so the high density of [OII]-selected galaxies may only reflect the higher than average density of matter in this region. The more interesting question is whether the star-formation histories of the [OII]-selected galaxies in Abell 851 are different from those of [OII]-selected galaxies drawn from the field. The [OII] equivalent widths are the best measure we have at this time of how quickly the star formation rate is changing in each galaxy.

The solid histogram in Figure 10 shows the distribution of EW_o for the on-band-selected galaxies. Most of the [OII]-selected galaxies in Abell 851 have equivalent widths less than $EW_o = 80 \text{ \AA}$, but the seven galaxies add a flat high-equivalent width extension to the distribution. The unusual sharpness of this break led us to wonder whether an entirely different population of galaxies was being detected at high equivalent width – namely

the $z \sim 3.31$ Ly α emitters. If so, the same population should be seen in our off-band selected sample. The open histogram in Figure 10 shows the emission-line equivalent widths of the off-band selected galaxies. Many more galaxies with equivalent-widths exceeding 100 \AA were detected in the off-band sample, and the distribution shows no discontinuity at 80 \AA . The emission-line galaxies are drawn from an off-band volume that is only two times larger than that of the cluster survey. High-redshift galaxies are known to be strongly clustered (Adelberger et al. 1998), but it seems contrived to explain the high number of large equivalent width galaxies in the off-band by invoking an overdensity of galaxies at high-redshift.

The straightforward explanation is that the high-equivalent population of [OII]-emitting galaxies has been removed from the cluster sample. Balogh et al. (1998) found that cluster galaxies brighter than $M_R \approx -18.3$ have lower [OII] equivalent widths than field galaxies of the same morphological type. A direct comparison to this work is difficult. In Figure 10 our off-band selected sample cuts off in the $EW_o \sim 20$ to 40 \AA interval instead of near 8 to 16 \AA like the on-band sample. Weak lines become harder to detect when they fall in W021, the off-band, instead of W022. The continuum flux density is more uncertain when measured in the narrower band, and this error is integrated over the broader bandpass when the continuum is subtracted. Detection at a fixed level of significance requires the line equivalent width to be a factor of two higher. The Balogh et al. sample of CNOC field and cluster galaxies contains no high equivalent width galaxies. We believe the difference mainly reflects our fainter magnitude limit. If the seven on-band galaxies with $EW_o > 100 \text{ \AA}$ are at the cluster redshift, their median absolute magnitude is only $M_{\lambda 3645}(AB) = -14$. Figure 8 of the Hogg et al. (1998) field survey shows the maximum [OII] equivalent widths increase with apparent magnitude. The relative paucity of cluster galaxies with $EW_e > 60 \text{ \AA}$ then reflects the recent suppression of star-formation in galaxies fainter than the Balogh et al. study reached. We do attribute the $EW_o > 400 \text{ \AA}$ off-band detections to Ly α interlopers,

and their absence in the on-band sample to the smaller volume.

4. Star Formation History of [OII]-Selected Galaxy Population

We have identified a population of star-forming galaxies near the cluster Abell 851 but commented little about the nature of the underlying galaxies. The types of star formation histories represented are investigated here and used to discuss the nature of the remnant populations in present-epoch clusters.

4.1. Star Formation Timescales

Figure 11 shows the observed equivalent widths and g-i colors of all the objects with an on-band excess. The [OII] luminosities of galaxies are empirically related to the number of massive stars born over the last few Myr, but the continuum emission near the line is dominated by stars with lifetimes of ~ 2 Gyr. Their ratio, the line equivalent width, measures the current star formation rate relative to the average SFR over the previous few Gyrs. The g-i color also provides some age discrimination because it spans the 4000 Å break of redshifted cluster galaxies. The strength of the break increases as stars of a few solar masses ascend the red giant branch and begin to dominate the continuum light, so the g-i color reddens about ~ 500 Myr after the stars form. A large range of both star formation timescales and population ages is required to explain the observed spread of equivalent width and color.

To describe the star-formation histories quantitatively, the population synthesis code developed by Babul & Ferguson (1996) and Madau et al. (1996) was used to build continuum spectra of stellar populations with different ages and star-formation histories. The continua were reddened using an empirical description of the star – dust geometry in

starburst galaxies (e.g. Calzetti 1997; Calzetti et al. 1996) and redshifted to $z = 0.4$. The g and i magnitudes were measured using the IRAF package SYNPHOT. The [OII] luminosity was estimated from the SFR parameter in each model using the relations described in § 2.3 and then attenuated for the assumed extinction, $A_B = 1.0$, using a Galactic extinction curve (Seaton 1979). These extinction corrections reduce the [OII] equivalent width by a factor of 0.65 because the starlight suffers less extinction than the nebular lines for the starburst geometry. The nebular continuum is not included in the current set of models. Four different star-formation histories are illustrated in Figure 11. The solid lines trace the aging population. Their absolute position would shift for different assumptions about the $L_{[\text{OII}]} / L_{\text{H}\alpha}$ ratio or A_B , but their overall shape serves to illustrate several important points.

The solid squares along the top line in Figure 11 follow a population with a constant star formation rate from an age of 4 Myr to 10 Gyr. The measured [OII] equivalent widths span a larger range than continuous star formation produces. The order of magnitude spread in their equivalent widths cannot be explained by extinction alone since some of the galaxies have very blue colors. The most obvious explanation is that the star formation rate in many of the galaxies is declining with time. The three evolutionary tracks below the constant SFR track illustrate the rapid decline in equivalent width with age when the star formation timescale is short. These stellar populations were created with an exponentially decaying SFR, $R = R_0 e^{-t/\tau}$, where $\tau = 10$ Myr, 100 Myr, and 1 Gyr from left to right. Decay timescales $\tau \sim 10$ Myr to infinity (i.e. continuous star formation) are needed to describe the range of colors and equivalent widths observed.

The equivalent width limit of our survey corresponds to a SFR at $z=0.4$ that is a few percent of the average SFR over a period $\sim 6\tau$. In other words, the stars that dominate the light from the $\tau = 10$ Myr models formed within the preceding ~ 60 Myr. It seems

reasonable to call them starburst galaxies. In contrast, the longest decay timescales, $\tau \sim 10^9$ yr, are similar to the gas consumption timescales in local spiral galaxies (e.g. Kennicutt 1983; Kennicutt, Tamblyn, & Congdon 1994). Intermediate timescales may reflect the slow removal of gas by processes specific to the cluster environment. Hence more than one physical process is believed to be responsible for producing the wide range of star formation timescales.

4.2. Bursting Dwarf Galaxies?

The 33 galaxies with the bluest g-i colors are highlighted by asterisks in Figure 11. They and a similar number of slightly redder, low equivalent width galaxies lie near the locus of $\tau = 10$ Myr models. The burst models redden slightly as their [OII] equivalent width decreases along this track. We will call these galaxies fading starburst galaxies. Most of them are fainter than the cluster population that has been cataloged and discussed previously (Dressler et al. 1999; Smail et al. 1997).

We can learn something about the stellar masses of the bursting galaxies from their luminosities. The best upper limit on their K-band luminosities – $K \approx 18.0$ (Stanford, Eisenhardt, & Dickinson 1995)⁸ – is not faint enough to be a useful mass constraint. Our reddest flux measurement, Sloan i , reflects the luminosity emitted in the rest-frame V band. The mass inferred from this luminosity depends on the star formation history adopted, so we have tried to illustrate the range of masses that could reasonably be assigned to each

⁸ Only 13 galaxies from the on-band excess sample were even detected in the infrared survey of Stanford, Eisenhardt, & Dickinson (1995), and seven of these galaxies were flagged as probable foreground interlopers. One galaxy has no color measurement, and the colors of the other 5 are between 1.6 and 2.0.

starburst galaxy in Figure 12. Models with a constant star formation rate cross the solid heavy line at the time when the total gas mass turned into stars is $10^9 M_\odot$. The 400 Myr old population with a SFR of $2.5 M_\odot \text{ yr}^{-1}$ is bluer and brighter than a population of the same mass and age that formed quickly. The fading sequence for a burst that formed 10^9 stars over $\tau = 10 \text{ Myr}$, for example, is shown by the heavy dashed line. After 10 Gyr, populations with a total stellar mass of $10^9 M_\odot$ lie along the dotted line connecting these two loci if their star-formation timescales are intermediate to the two extremes illustrated. Congruent loci for $10^8 M_\odot$, $10^{10} M_\odot$, and $10^{11} M_\odot$ populations are outlined on the color – magnitude diagram. Comparison of the $10^9 M_\odot$ fading-burst track to the $10^{10} M_\odot$ constant SFR track clearly shows that galaxies at a given magnitude and color will be assigned a lower stellar mass if a fading burst model rather than a constant SFR model is invoked. The interesting point is that the upper limit on the masses of the bluest starburst galaxies is only $10^9 M_\odot$, and the best estimate of the stellar mass involved in the burst is closer to $10^8 M_\odot$ models. These galaxies could be dwarf galaxies.

The dwarf galaxy candidates are smaller than a typical [OII]-selected galaxy. At the detection threshold, the isophotal area of a galaxy with $g-i < 1.0$ is typically a factor of two smaller than one with $1.0 < g-i < 2.0$. This trend reflects a tighter underlying correlation between size and magnitude. All of the faint galaxies are small, but few of the brighter [OII]-selected galaxies have an extremely blue $g-i$ color. We detect cluster galaxies in their rest-frame U band, so *size* here is understood to imply *size of the star-forming region*. The nearly linear correlation between size and flux implies the star-forming regions in the dwarfs have the same central surface brightness but smaller scale length than the brighter galaxies. These bursts of star-formation activity may briefly outshine an older stellar population without contributing much to the galaxy’s total stellar mass. Gas-phase metallicity measurements will be the best way to confirm or refute the dwarf-identity of these galaxies. We note that the oxygen abundances recently measured for a few compact

galaxies in Cl 0024+16 implied higher stellar masses than either the luminosities or line widths of those galaxies revealed (cf. Kobulnicky et al. 1999; Koo et al. 1997).

4.3. Implications for the Formation of the Dwarf Galaxy Population in Clusters

If the low [OII] equivalent widths of the cluster galaxies relative to galaxies in the field is taken as evidence that the SFR’s in the cluster galaxies are declining faster than normal, then some environmental process must be removing gas from them. The physical cause of the gas removal is still unclear, but galaxy harrassment appears to be consistent with the lack of a strong clustercentric gradient in galaxy properties and a broad range of decay timescales for the SFR (Moore et al. 1996).

Most of the short bursts appear to have taken place in dwarf galaxies. The luminosity of their remnants depends quite strongly on the star formation history before and after the luminous burst. However, the maximum fading rate of the bursting galaxies and their minimum remnant luminosities follow directly from the SFR and birthrate parameter measured at $z=0.4$. Such fading starbursts have been discussed frequently in the literature as a means of lowering the luminosity of prominent high-redshift galaxies below detection limits by the current epoch (Phillipps & Driver 1995; Ferguson & Babul 1998). The R-band absolute magnitudes of remnants produced by the star formation histories defined in § 4.1 are compared in Table 4. A bursting dwarf galaxy with a SFR of $0.1 M_{\odot} \text{ yr}^{-1}$ at $z = 0.4$ has faded to $M_R = -10.13$ to -9.6 by the present epoch, and this range represents metallicities from $0.02 Z_{\odot}$ and $1.0 Z_{\odot}$. In contrast, if small bursts propagate over the galaxy such that the galactic SFR is nearly constant at $0.1 M_{\odot} \text{ yr}^{-1}$, then the remnant’s luminosity increases to $M_R = -16.55$ to -17.73 for the same metallicity interval. We cannot directly distinguish between these two scenarios because it is not possible to constrain the number of bursts in

an individual object with the present data.

In spite of the limited information, it is interesting to compare models for the luminosity distribution of the remnants to the dwarf population in nearby galaxy clusters. Since Abell 851 is a richer cluster than Virgo, a plausible model should produce at least as many dwarfs of a given type as are found in the Virgo Cluster Catalog, VCC (Sandage et al. 1985). The VCC lists 34 blue compact dwarfs, over 100 dwarf irregular galaxies, and about 200 spiral galaxies. These numbers are not very different from the number of blue, compact galaxies (33) and moderately blue galaxies (160) that we found in Abell 851. However, the star formation rates in the [OII]-selected galaxies cannot remain constant at their $z = 0.4$ rate. Most of the [OII]-selected galaxies, i.e. those with moderately blue g-i color, would become as luminous as the spiral galaxy population in Virgo. While this constant star formation rate scenario does not produce too many spiral galaxies, it does predict $z = 0$ star formation rates that are higher than those of typical Virgo cluster spiral galaxies. Also, nearly half of the galaxies in Table 1 would be brighter than the VCC dwarf galaxies, so the progenitors of the Virgo dwarf population would remain unidentified. In contrast, the declining star formation rates in Abell 851 galaxies suggested by our analysis of their color and equivalent width distribution produces many more dwarf galaxy remnants. We would only classify a galaxy as a burst during a 60 Myr period, so the number of remnants from galaxies that undergo a starburst over the ~ 7 Gyr period from redshift zero to $z = 1$ could be two orders of magnitude larger than number directly detected.

For purposes of illustration, we assume the main star-formation episode has been detected in the [OII]-selected galaxies. Which remnants would then have luminosities similar to the dE population in clusters at the present epoch? The top panel and middle panel of Figure 13 illustrate the remnants of the population that was [OII]-selected at $z=0.4$ with $g-i < 2.0$. Many galaxies assigned short, $\tau = 10$ Myr, SFR decay timescales would have

faded below the detection limit of the VCC, and most galaxies brighter than $M_R = -13$ would be descendents of the population with a slower suppression of the SFR. These galaxies had redder g-i colors at $z=0.4$ similar to spiral galaxies, so the implication is that many of the dE-progenitors underwent multiple generations of star-formation. These more luminous progenitors may not create a metallicity problem for the remnants. The J-K colors of some Virgo dE's indicate fairly high metallicities (Bothun et al. 1985), and a metallicity range from $0.02 Z_\odot$ to $1.0 Z_\odot$ would produce a range of $b - r$ colors consistent with the color spread observed among the dE galaxies in the Coma cluster (Secker & Harris 1996).

The problem with forming stars late ($z < 1.0$) in dE progenitors seems to be producing enough remnants. The bottom panel of Figure 13 illustrates the situation. The dE population was assumed to form in the cluster between $z = 1.0$ and $z = 0.4$. The histograms for the three star formation timescales shown in the middle panel were then scaled by their respective duty cycle corrections. Galaxies with star formation timescales ~ 10 Myr produce more remnants than those with longer star formation timescales when the remnant population is boosted by the duty cycle correction. However, the total number of gas-depleted remnants in each magnitude bin, dotted line, is still less than the estimated number of Virgo dE's, solid line.⁹ Over the range from $-18 < M_R < -13$, only 277 remnants are produced whereas the VCC lists about 1000 dE galaxies in this magnitude range. To resolve the numbers problem the progenitors of dE galaxies would need to form stars over a longer period from $z \sim 2$ to $z \approx 0$ (yielding over 800 remnants in the above magnitude range). Perhaps this period reflects the timescale over which the cluster environment has been able to suppress the star formation activity of infalling galaxies.

In summary, our impression is that Abell 851 does not contain enough bursting dwarf

⁹ We have assumed a distance to the Virgo Cluster of 17.0 Mpc and a mean B-R color of 1.32 since the VCC lists only B magnitudes.

galaxies to form a large dE galaxy population by the present epoch. Either many dE progenitors are not dwarf galaxies or one of two scenarios holds. First, it cannot be ruled out that the dwarf galaxies in Abell 851 went through a bursting phase at an earlier epoch, prior to $z = 0.4$. This solution is unsatisfying unless it can be connected to some dynamical aspect of cluster assembly. Second, we assumed the dwarf galaxies experienced only a single burst of star formation activity. In a more realistic model where dwarf galaxies burst multiple times, the remnants will be brighter. Although their duty cycle is also larger in this scenario, the net number of detectable remnants can be increased over the single-burst scenario. It is likely that our [OII]-selected population includes more than one type of dE progenitor – the dwarf galaxies which have undergone these multiple episodes of star formation and some brighter, spiral galaxies which will be partially disrupted by tidal interactions. Despite the large number of dwarf and spiral galaxies with declining star formation rates in Abell 851, an extended period $\sim 8 - 9$ Gyr seems to be required to build up the dE population.

5. Summary

We presented a deep, emission-line-sensitive image of the galaxy cluster Abell 851. Galaxies with strong [OII] $\lambda\lambda 3726, 29$ emission ($EW_o \gtrsim 11$ Å) were detected to $m_{5129}(AB) = 24.0$. Foreground galaxies with steep breaks in the spectral continuum near 4000 Å contaminate the sample selected by on-band excess flux. We showed, however, that such interlopers will have very red g-i colors and excluded 123 on-band-selected galaxies with red colors from the sample of 248 probable [OII] emitters. We argued that high-redshift galaxies with extremely strong Ly α emission must contaminate the sample, but the differences between the equivalent width distributions of the on-band-selected and off-band-selected samples lead us to believe most lines with $EW_o < 400$ Å (i.e.

$EW_e < 285 \text{ \AA}$) are [OII] detections.

Many of the [OII]-selected galaxies are too faint to have previously measured redshifts. We constrain their redshifts to the interval $0.399 < z < 0.415$, which includes cluster members with peculiar velocities from -1474 km s^{-1} to 1450 km s^{-1} and field galaxies within several tens of Mpc of the cluster along our sightline. Their co-moving density is at least several times higher than that of [OII]-selected field galaxies at similar redshifts (Cowie et al. 1997; Hogg et al. 1998). Hence the [OII]-selected population appears to be associated with the overdensity of galaxies that defines the cluster even though their projected spatial distribution is less centrally concentrated than the general cluster population. We suspect the extra star-forming galaxies are associated with infalling galaxies over scales $\gtrsim 2 \text{ Mpc}$, the radius of our field of view.

The star-formation episodes within individual galaxies are not as strong on-average as the bursts seen in the field population. The cluster galaxies have lower equivalent widths than [OII]-selected field galaxies. The range of equivalent widths and g-i colors among cluster galaxies is significantly larger than differences in intrinsic reddening and/or excitation (i.e. the scatter in the [OII]- $H\alpha$ relation) can easily explain. We believe galaxies with very different types of star-formation histories are represented in the [OII]-selected population. We used population synthesis models to demonstrate that the star formation timescales in two-thirds of the [OII]-selected sample are of order a few times 10^8 to 10^9 yr . These galaxies have moderately blue colors similar to normal spiral galaxies, and the high end of this range is consistent with the gas consumption timescales in field spirals (Kennicutt et al. 1994; Kennicutt 1983). The intermediate timescales may reflect the slow removal of gas by the cluster, but we regard these timescales tentatively until confirmed using other spectral diagnostics less sensitive to reddening. In contrast, the star-formation timescale of at least 13%, and possibly of as many as one third, of the galaxies is distinctly

shorter. These galaxies are very blue ($g-i < 1.0$), and we believe they are starburst galaxies.

While the luminosity of these starburst galaxies is clearly dominated by a young population of stars, estimates of their total stellar mass are highly uncertain because the star formation history more than a few Gyr prior to the $z \sim 0.4$ epoch is not well constrained by the available data. Nonetheless the mean i-band magnitude of the starburst population is ~ 2 magnitudes fainter than that of the spiral-like population, and the absolute luminosities of the starburst galaxies range from $M(AB) \approx -18$ to -14 (rest-frame U band). Their stellar masses could be as low as 10^8 to $10^9 M_\odot$, so we suggest they are bursts of star formation in dwarf galaxies. A preliminary discussion of the sizes of these galaxies showed they were among the most compact objects selected as [OII]-emitting galaxies. Spectroscopic observations will yield metal abundances and absorption-line strengths for this population which will reveal their true nature.

We find there simply are not enough of these small starbursts to form all of the dE's seen in nearby clusters via a wind-driven transformation of gas-rich dwarfs into dE galaxies. The bursting dwarfs do form an important subset of a larger population of [OII]-selected galaxies which must significantly decrease their SFR's by the current epoch however. Otherwise far more bright spirals and irregulars would be found in clusters today. We have caught these [OII]-selected galaxies at a stage when their SFR is declining faster than it would in the field. While their projected spatial distribution is not as centrally concentrated as the nucleated dE population in the Virgo Cluster, the density contrast across our field of view is very similar to that measured for the bright dE population in the Virgo cluster over comparable length scales (Binggeli et al. 1987; Ferguson & Sandage 1989). Our analysis certainly suggests then that dwarf elliptical galaxies were forming in clusters at $z \approx 0.4$.

We thank Ed Carder of KPNO for measuring the filter transmission curves and simulating their response in the f/3.14 beam prior to our run. We express our sincere

thanks to Daniela Calzetti for illuminating discussion about the impact of dust on the [OII] equivalent width. We would to thank the Morphs group (Dressler, Oemler, Couch, Ellis, Poggianti, Barger, Butcher, Sharples, Smail) for creating an easily accessible WWW interface to their Abell 851 spectra. This work was supported by NASA through Hubble Fellowship grant HF-01083.01-96A awarded by the Space Telescope Science Institute, which is operated by the Association of Universities for Research in Astronomy, Inc., for NASA.

REFERENCES

- Adelberger, K. L. et al. 1998, *ApJ*, 505, 18.
- Babul, A. & Ferguson, H. C. 1996, *ApJ*, 458, 100.
- Balogh, M. et al. 1997, *ApJ*, 488, 75.
- Balogh, M. et al. 1998, *ApJ*, 504, 75.
- Belloni, P. & Roeser, H.-J. 1996, *A&AS*, 118, 65.
- Bertin, E. & Arnouts, S. 1996, *A&AS* 117, 393.
- Binggeli, B., Tammann, G. A., & Sandage, A. 1987, *AJ*, 94, 251.
- Bothun, G. D., Mould, J. R., Wirth, A., & Caldwell, N. 1985, *AJ*, 90, 697.
- Bothun, G. D. et al. 1986, *AJ*, 92, 1007.
- Butcher, H., & Oemler, A 1978, *ApJ*, 219, 18.
- Calzetti, D. 1997, *AJ*, 113, 162.
- Calzetti, D., Kinney, A. L, & Storchi-Bergmann, T. 1996, *ApJ*, 458, 132.
- Coleman, Wu, & Weedman 1980, *ApJS*, 43, 393.
- Cowie, L. L., Songaila, A., Hu, E. M., & Cohen, J. G. 1996, *AJ*, 112, 839.
- Cowie, L. L., & Hu, E. M. 1998, *AJ*, 115, 1319.
- Dressler, A., Gunn, J. E. 1982, *ApJS*, 78, 1.
- Dressler, A. et al. 1994, *ApJ*, 435, 23.
- Dressler, A. et al. 1999, *ApJS*, 78, 1.
- Driver, S. P. et al. 1994, *MNRAS*, 268, 393.
- Ferguson, H. C. & Babul, A. 1998, *MNRAS*, 296, 585.
- Ferguson, H. C., & Binggeli, B. 1994, *ARA&A*, 6, 67.

- Ferguson, H. C. & Sandage, A. 1989, ApJ, 346, L53.
- Ferguson, H. C. & Sandage, A. 1991, AJ, 101, 765.
- Fukugita, M. et al. 1996, AJ, 111, 1748.
- Gallagher, J. S., Bushouse, H., Hunter, D.A. 1989, AJ, 97, 700.
- Gallego, J., Zamorano, J., Aragon-Salamanca, A., & Rego, M. 1995, ApJ, 455, 1.
- Grebel, E. K. 1997. Review of Modern Astronomy 10:29-60.
- Grebel, E. K. 1998, in Dwarf Galaxies and Cosmology
- Gronwall, C. 2000, pvt comm.
- Hu, E. M., Cowie, L. L., & McMahon, R. G. 1998, ApJ, 502, 99.
- Hogg, D. W., Cohen, J. G., Blandford, R., & Pahre, M. A. 1998, ApJ, 504, 622.
- Hammer, F. et al. 1997, ApJ, 481, 49.
- Jones, L. R. et al. 1991, MNRAS, 249, 481.
- Jorgensen, I. 1994 ApJ, 433, 553.
- Kennicutt, R. C. 1983, ApJ, 272, 54.
- Kennicutt, R. C. 1992a, ApJ, 388, 310.
- Kennicutt, R. C. 1992b, ApJS, 79, 255.
- Kennicutt, R. C., Tamblyn, P., & Congdon, C. W. 1994, ApJ, 435, 22.
- Kobulnicky, H. A. & Zaritsky, D. 1999, ApJ, 511, 118.
- Koo, D. C., Guzman, R., Gallego, J., & Wirth, G. 1997, ApJ, 478, 49.
- Leitherer, C. et al. 1999, preprint astro-ph/9902334.
- Lilly, S. J. et al. 1995, ApJ, 455, 108.
- Lotz, J., Martin, C. L., & Ferguson, H. 2001, in prep.

- Loveday et al. 1999, MNRAS, 310, 262.
- Mac Low, M.-M. & Ferrara, A. 1999, ApJ, 513, 142.
- Madau, P. 1995, ApJ, 441, 18.
- Martin, C. L. 1997, ApJ, 491, 561.
- Martin, C. L. 1998, ApJ, 506, 222.
- Martin, C. L. 1999, ApJ, 513, 156.
- Mateo, M. 1998, Ann Rev A&A, 36, 435.
- Moore, B., Katz, N., Lake, G., Dressler, A., & Oemler, A. 1996, Nature, 379, 613.
- Phillipps, S. & Driver, S. 1995, MNRAS, 274, 832.
- Sadat, R., Blanchard, A., & Oukbir, J. 1998, A&A, 329, 21.
- Salzer, J. J. 1989, ApJ, 347, 152.
- Sandage, A., Binggeli, B., & Tammann, G. A. 1985, AJ, 90, 1759.
- Schindler, S. & Wambsganss, J. 1996, A&A, 313, 113.
- Schaller, G., Schaerer, D., Meynet, F. et al. Maeder, A. 1992, A&AS, 96, 269.
- Seaton, M. J. 1979, MNRAS, 187, 73.
- Secker, J. & Harris, W. E. 1996, ApJ, 469, 623.
- Smail, I. et al. 1997, ApJS, 110, 213.
- Smecker-Hane, T. A. et al. 1994, AJ, 108, 507.
- Steidel, C. C. et al. 1998, 492, 428.
- Steidel, C. C. et al. 1999a, ApJ, 519, 1.
- Steidel, C. C. et al. 1999b, astro-ph/9910144.
- Standford, S. A., Eisenhardt, P. R., & Dickinson, M. 1995, ApJ, 450, 512.

- Sullivan, M. O. et al. , astroph-9910104.
- Thuan, T. X., 1985, ApJ, 299, 881.
- Trentham, N. 1997a, MNRAS, 286, 133.
- Trentham, N. 1997b, MNRAS, 290, 334.
- Trentham, N. 1998, MNRAS, 293, 71.
- Tresse, L, & Maddox, S. J. 1998, ApJ, 495, 691.
- Tresse, L, Maddox, S., Loveday, J., & Singleton, C. 1999, MNRAS, 310, 262.
- White, S. D. M., Efstathiou, G., & Frenk, C. S. 1993, MNRAS, 262, 1023.
- Wilson et al. 1997, MNRAS, 287, 415.

Table 1. Emission-Line Candidates with Blue Colors

ID#	X	Y	RA	DEC	$T_\lambda F$	F_λ	g
	(pix)	(pix)	(j2000)	(j2000)	(ergs s ⁻¹ cm ⁻²)	(ergs s ⁻¹ cm ⁻² Å ⁻¹)	(mag)
2413	939.58	832.64	09:42:59.528	+46:57:27.68	$9.53 \pm 0.58 \times 10^{-17}$	1.41×10^{-18}	23.71 ± 0
5706	1115.7	1258.42	09:42:52.381	+47:00:24.01	$1.180 \pm 0.073 \times 10^{-16}$	1.99×10^{-18}	23.43 ± 0
4230	764.56	1423.8	09:43:06.763	+47:01:32.23	$1.258 \pm 0.078 \times 10^{-16}$	2.07×10^{-18}	23.45 ± 0
368	1024.44	130.81	09:42:56.013	+46:52:40.81	$1.38 \pm 0.11 \times 10^{-16}$	3.54×10^{-18}	22.93 ± 0
756	525.94	265.14	09:43:16.228	+46:53:34.91	$1.81 \pm 0.15 \times 10^{-16}$	4.98×10^{-18}	22.59 ± 0
281	1491.63	96.78	09:42:37.113	+46:52:28.03	$9.01 \pm 0.75 \times 10^{-17}$	2.18×10^{-18}	23.4 ± 0
5740	21.04	1269.62	09:43:37.124	+47:00:27.58	$1.19 \pm 0.10 \times 10^{-16}$	3.23×10^{-18}	23.05 ± 0
773	930.19	273.34	09:42:59.844	+46:53:38.57	$6.01 \pm 0.64 \times 10^{-17}$	1.55×10^{-18}	23.88 ± 0
3392	1881.27	1124.57	09:42:21.137	+46:59:30.07	$3.89 \pm 0.47 \times 10^{-17}$	1.02×10^{-18}	24.65 ± 0
3157	1595.69	1056.04	09:42:32.786	+46:59:01.07	$8.1 \pm 1.0 \times 10^{-17}$	3.43×10^{-18}	22.92 ± 0
522	916.12	192.5	09:43:00.405	+46:53:05.69	$5.11 \pm 0.65 \times 10^{-17}$	1.71×10^{-18}	23.85 ± 0
2303	955.22	803.64	09:42:58.887	+46:57:15.76	$1.76 \pm 0.29 \times 10^{-17}$	4.5×10^{-19}	25.32 ± 0

Table 1—Continued

ID#	X	Y	RA	DEC	T_λ F	F_λ	g
	(pix)	(pix)	(j2000)	(j2000)	(ergs s ⁻¹ cm ⁻²)	(ergs s ⁻¹ cm ⁻² Å ⁻¹)	(mag)
5269	1787.81	1757.03	09:42:24.896	+47:03:52.52	$2.13 \pm 0.397 \times 10^{-17}$	8.1×10^{-19}	$25.34 \pm 0.$
3954	358.89	1344.21	09:43:23.341	+47:00:58.74	$1.38 \pm 0.25 \times 10^{-17}$	3.2×10^{-19}	$25.99 \pm 0.$
824	885.24	301.2	09:43:01.670	+46:53:49.86	$1.86 \pm 0.37 \times 10^{-17}$	6.8×10^{-19}	$24.77 \pm 0.$
459	1931.46	167.47	09:42:19.316	+46:52:58.12	$4.51 \pm 0.93 \times 10^{-17}$	3.18×10^{-18}	$22.78 \pm 0.$
4829	938.56	1645.91	09:42:59.673	+47:03:04.92	$2.68 \pm 0.62 \times 10^{-17}$	1.88×10^{-18}	$23.58 \pm 0.$
889	909.21	328.	09:43:00.702	+46:54:00.81	$9.3 \pm 2.3 \times 10^{-18}$	2.6×10^{-19}	$26.22 \pm 0.$
2711	941.76	923.98	09:42:59.450	+46:58:05.35	$4.31 \pm 1.07 \times 10^{-17}$	3.87×10^{-18}	$22.85 \pm 0.$
89	1811.27	25.84	09:42:24.211	+46:52:00.38	$1.93 \pm 0.48 \times 10^{-17}$	1.17×10^{-18}	$24.89 \pm 0.$
5066	1953.46	1736.64	09:42:18.121	+47:03:44.31	$9.39 \pm 2.42 \times 10^{-17}$	9.48×10^{-18}	$22.00 \pm 0.$
2334	351.07	809.65	09:43:23.497	+46:57:17.71	$1.79 \pm 0.47 \times 10^{-17}$	1.09×10^{-18}	$24.43 \pm 0.$
2524	663.91	875.69	09:43:10.769	+46:57:45.12	$1.33 \pm 0.35 \times 10^{-17}$	6.3×10^{-19}	$24.72 \pm 0.$
3815	1055.11	1256.43	09:42:54.858	+47:00:23.10	$8.7 \pm 2.3 \times 10^{-18}$	3.0×10^{-19}	$25.72 \pm 0.$

Table 1—Continued

ID#	X	Y	RA	DEC	T_λ F	F_λ	g
	(pix)	(pix)	(j2000)	(j2000)	(ergs s ⁻¹ cm ⁻²)	(ergs s ⁻¹ cm ⁻² Å ⁻¹)	(mag)
737	1134.09	272.67	09:42:51.580	+46:53:38.61	$1.04 \pm 0.28 \times 10^{-17}$	4.0×10^{-19}	25.63 ± 0.2
508	944.84	188.9	09:42:59.241	+46:53:04.27	$1.54 \pm 0.42 \times 10^{-17}$	8.1×10^{-19}	24.90 ± 0.2
1118	701.44	405.99	09:43:09.144	+46:54:32.41	$9.4 \pm 2.7 \times 10^{-18}$	3.8×10^{-19}	25.69 ± 0.2
3733	1483.21	1227.03	09:42:37.367	+47:00:11.63	$1.60 \pm 0.46 \times 10^{-17}$	1.09×10^{-18}	24.39 ± 0.2
4319	168.76	1449.74	09:43:31.150	+47:01:42.41	$1.65 \pm 0.47 \times 10^{-17}$	1.11×10^{-18}	24.27 ± 0.2
1889	1269.36	671.82	09:42:46.092	+46:56:22.06	$7.0 \pm 2.0 \times 10^{-18}$	1.7×10^{-19}	26.0 ± 0.3
2987	930.6	992.86	09:42:59.913	+46:58:33.78	$1.96 \pm 0.58 \times 10^{-17}$	1.33×10^{-18}	24.02 ± 0.2
1337	160.92	473.73	09:43:31.105	+46:54:59.95	$1.82 \pm 0.55 \times 10^{-17}$	1.43×10^{-18}	24.30 ± 0.2
2196	551.66	765.95	09:43:15.316	+46:56:59.84	$1.95 \pm 0.61 \times 10^{-17}$	1.80×10^{-18}	23.42 ± 0.2

Table 2: Comparison to Spectroscopic Subsample^a

N_{gal}	N_{gal}	Description
D99	this paper	
71		Identified as Cluster Members ^a
19		Detected [OII] in Spectrum ^a
	8	Identified as [OII] Candidates ^b
	4	Redshifted beyond filter bandpass. ^b
	6	Equivalent width less than (12\AA) . ^b
	1	Unusual emission-line spectrum. ^c
52		No [OII] Detected in Spectrum ^a
	45	No on-band excess detected
	5	On-band excess significant. Too red ($g - i > 2.0$) for EL galaxy sample (4); $g - i = 1.79 \pm 0.28$ (1).
	2	Detected but not extracted by SE.
66		Classified as field galaxies. ^a
	59	No on-band excess ^b
	3	Significant on-band excess. Too red for EL sample (2) and one with $g - i = 1.71 \pm 0.28$.
	3	Detected but not extracted by SE.
	1	Miss-classified as a star.

^aDressler et al. 1999.

^bThis paper.

^cThe [OII] equivalent width should be easily detected, yet we measured a negative line flux. See text for details.

Table 3: Distribution of [OII] Emission-Line Fluxes

$\log(T_\lambda F_l)^a$	\dot{M}^b	N^c	N_{oi}^d	C_f^e	η^f
-15.25	5.30	17	9	1.02 ± 0.02	$6.7(\pm 2.2) \times 10^{-3}$
-15.75	2.00	62	42	1.05 ± 0.03	$3.2(\pm 0.5) \times 10^{-2}$
-16.25	0.53	107	71	1.10 ± 0.03	$5.7(\pm 0.7) \times 10^{-2}$
-16.75	0.17	147	91	2.63 ± 0.9	0.17 ± 0.06

^aMeasured line flux in $\text{ergs s}^{-1} \text{ cm}^{-2}$. These values must be divided by the filter transmission at the wavelength of the line.

^bEstimated star formation rate in $\text{M}_\odot \text{ yr}^{-1}$. See text for details.

^cTotal number of 3σ detections.

^dNumber of objects in column 3 which are likely to be detections of [OII] emission. The 123 galaxies with red g-i colors and the 7 galaxies with equivalent widths exceeding 100\AA are excluded.

^eIncompleteness correction. Each galaxy was assigned a detection probability, f_i , interpolated from a grid of Monte Carlo simulations. The average correction for each bin, $1/N \sum 1/f_i$, is given. The error bars represent the uncertainty in this interpolation or the Poisson noise, whichever is larger.

^fNumber of emission-line galaxies per $\text{Mpc}^{-3}/0.5 \text{ mag}$ ($H_0 = 70 \text{ km s}^{-1} \text{ Mpc}^{-1}$, $\Omega_M = 0.2$, and $\Omega_\lambda = 0$).

Table 4: Population Synthesis Models^a

τ^b	$t_o(0.4)$	g-i	EW_o	$t_o(0)$	0.02 Z_\odot	0.2 Z_\odot	1.0 Z_\odot
Myr	Myr	mag	\AA	Gyr	b-r, M_R	b-r, M_R	b-r, M_R
10	20	0.48	93	4	1.05, -10.13	1.29, -9.88	1.59, -9.6
10	40	0.69	30	4	1.05, -10.13	1.29, -9.88	1.59, -9.6
10	60	0.91	7	4	1.05, -10.13	1.29, -9.88	1.59, -9.6
100	200	1.02	65	4	1.06, -12.64	1.29, -12.39	1.60, -12.1
100	400	1.61	25	4	1.06, -12.64	1.29, -12.39	1.60, -12.1
100	600	2.00	7	4	0.95, -15.49	1.29, -12.39	1.60, -12.1
1000	2000	1.71	53	4	0.95, -15.49	1.11, -15.26	1.28, -14.95
1000	4000	2.35	26	8	0.95, -15.49	1.35, -19.47	1.62, -19.05
1000	6000	2.82	9	8	1.13, -19.73	1.35, -19.47	1.62, -19.05
inf	10^4	1.64	68	14	0.78, -16.55	0.88, -18.00	0.93, -17.73

^a All models include an intrinsic reddening of $A_B = 1.0$ magnitude and are normalized to a star formation rate of $0.1 \text{ M}_\odot \text{ yr}^{-1}$.

^bCol. 1 – The decay timescale for the star formation rate where the rate is $R = R_0 e^{-t/\tau}$. Col. 2 – The age of the stellar population at redshift 0.4. Col. 3, 4 – The color and [OII] emission line equivalent width measured in the observer’s frame. Col. 5 – The age of the stellar population at redshift zero. Col. 6 - 11 – The color and absolute magnitude of the remnant for three values of the metallicity.

Fig. 1.— Filter transmission in the f/3.14 beam. The bandpass of filter W022, our *on band*, includes [OII] $\lambda\lambda 3726, 29$ emission at the cluster redshift. We estimate the continuum level from the flux measured in W021, our *off band*.

Fig. 2.— The central region of the co-added narrow band images. The lower left corner of this panel has coordinates (659,659) in the system of image coordinates used in Table 1. Tickmarks are shown at 20 pixel intervals. Galaxies with an on-band excess at the $S/N \geq 3$ level are marked according to their g-i color – g-i < 1.0 (open squares), $1.0 < \text{g-i} < 2.0$ (open circles), $\text{g-i} > 2.0$ (X's), and poorly measured color (open triangles). Galaxies with a flux excess in the off-band are only indicated if their color falls in the bluest bin (open squares with an X). The other 8 panels of the field can be viewed at <http://astro.caltech.edu/~clm/dwoii.html>.

Fig. 3.— Star – galaxy separation. Filled circles denote objects classified as stars based on their area (at a specified surface brightness) and flux.

Fig. 4.— Signal-to-noise ratio of the on-band excess vs. continuum flux. The sensitivity of our survey to emission lines in the on band is shown by the solid lines for four galaxy models: (a) emission-line equivalent width of 300 Å and area of nine pixels, (b) emission-line equivalent width of 60Å and area of nine pixels, (c) emission-line equivalent width of 60Å and area of 200 pixels, and (d) emission-line equivalent width of 11Å and area 200 pixels. A selection cut at $S/N = 4$ is equivalent to an equivalent width cut at 11Å for small galaxies with $\log F_\lambda = -18$ which is $m_{5129}(AB) = 24.0$. The dotted line at $S/N = 3$ illustrates the selection criterion used for Table 1.

Fig. 5.— On-band flux excess vs continuum flux density at $\lambda 5129$. The diagonal lines show locii of constant equivalent width at 100, 60, and 20 Å, from top to bottom, for reference. The signal-to-noise level of the limiting on-band flux excess shown, $S/N \geq 3$ in this case, produces the envelope at low equivalent widths. The dotted lines illustrate our completeness limits for detection and are labeled with the fraction of galaxies detected along that locus. The symbols denote the broadband g-i color of each galaxy (see key in figure).

Fig. 6.— Response of our filters to Coleman (1980) spectral templates versus redshift. The solid, dotted, and dashed lines represent the SED of an E/S0, Sbc, and Im galaxy respectively. (*Bottom*) The on-band excess created for each spectrum as a function of redshift. (*top*) The g-i color versus redshift. Intergalactic attenuation is included.

Fig. 7.— Equivalent measured from narrowband images (this paper) versus equivalent width measured spectroscopically (Dressler et al. 1999).

Fig. 8.— Distribution of star formation rates. Circles represent our Abell 851 results. Triangles show the field at $z \sim 0.4$ (Hogg et al. 1998). The cluster and field data have been converted to a SFR using $L_{H\alpha}$ (observed) $\approx 1.17 L_{[OII]}$ (observed) and the relation $\dot{M}_* = L_{H\alpha} E_{H\alpha} / 1.36 \times 10^{41} \text{ergs/s}$. The $H\alpha$ luminosity is assumed to be attenuated by a factor of 1.75, corresponding to $A_B = 1.0$ (Seaton 1979). For comparison, the local $H\alpha$ luminosity functions from Gallego et al. and Tresse et al. are shown. All results are scaled to $H_0 = 70 \text{ km/s/Mpc}$, $\Omega_M = 0.2$, and $\Omega_\lambda = 0$.

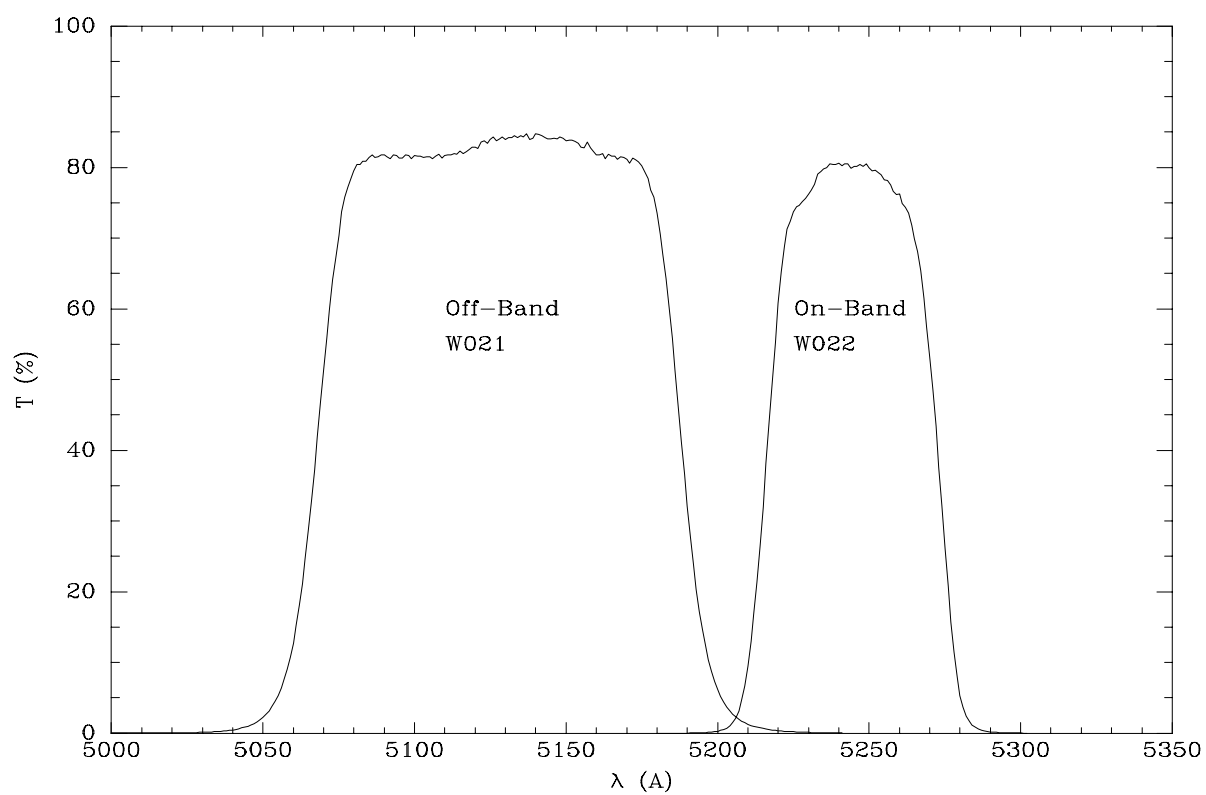
Fig. 9.— Spatial distribution of objects with an on-band flux excess (top row) and an off-band flux excess (bottom row). The x and y axes have tickmarks at 100 pixel intervals. The spatial distributions are shown separately for galaxies with blue, green, and red g-i color.

Fig. 10.— Distribution of [OII] equivalent-widths for the Abell 851 sample (solid bars) and the field sample (open bars). For cluster members, the rest-frame equivalent widths are a factor of ~ 1.4 lower.

Fig. 11.— Observed equivalent width versus color relation for the on-band-selected sample. Galaxies with large color errors are shown by open squares at $g-i=0$. The Xs denote galaxies in which the on-band excess is not attributed to line emission. The evolution of a galaxy is illustrated for four star formation histories. A stellar population with a constant SFR is shown at ages of 4 Myr, 40 Myr, 400 Myr, 1 Gyr, and 10 Gyr by from left to right by the solid squares. The three sequences below illustrate a SFR that declines by a factor of 0.37 over 10 Myr, 100 Myr, and 1 Gyr. The stellar population along each fading track is shown at ages of τ , 2τ , 4τ , and 6τ (from top to bottom). All models include an internal extinction of $A_B = 1.0$ magnitude.

Fig. 12.— Color – magnitude diagram for the on-band-selected galaxies. Asterisks and circles denote the starburst population and the [OII]-emitters with intermediate colors, respectively. The fraction of interlopers without [OII] emission is likely higher in the redder population represented by the X's. The heavy lines outline the region populated by modeled stellar populations that contain $10^9 M_\odot$ of stars (see text for details). Congruent locii are indicated for $10^8 M_\odot$, $10^{10} M_\odot$, and $10^{11} M_\odot$ populations. The models have been reddened with a Galactic extinction law assuming $A_B = 1.0$ mag.

Fig. 13.— Remnants of the [OII]-selected galaxies in Abell 851 at $z \sim 0$. A single-burst scenario is assumed for purposes of illustration. *Top:* Number - absolute magnitude relation. The galaxies with $g-i < 1.0$ and those with $1.0 < g-i < 2.0$ populate the solid and open histograms respectively. *Middle:* Same as top panel, but the histogram shading depicts star formation timescale instead of color; from left to right τ equals 1 Gyr, 100 Myr, and 10 Myr. *Bottom:* Duty-cycle correction. For this illustration, we assumed each galaxy bursts only once and that bursts occur at a constant rate in the cluster between redshifts $z \sim 1.0$ and $z \sim 0.4$. The dashed line illustrates the total number of remnants from the [OII]-selected population. The solid line represents the magnitude distribution of galaxies classified as dwarf ellipticals in the VCC.



This figure "f2.gif" is available in "gif" format from:

<http://arxiv.org/ps/astro-ph/0005534v1>

This figure "f3.gif" is available in "gif" format from:

<http://arxiv.org/ps/astro-ph/0005534v1>

